THE JOURNAL OF PHYSICAL CHEMISTRY C

pubs.acs.org/JPCC Article

Large-Scale Molecular Dynamics Simulation of the Dehydration of a Suspension of Smectite Clay Nanoparticles

Thomas R. Underwood* and Ian C. Bourg*

Cite This: J. Phys. Chem. C 2020, 124, 3702−3714 Read Online

ACCESS | Metrics & More | Article Recommendations | Supporting Information

ABSTRACT: Fine-grained sediments and sedimentary rocks play important roles in a variety of modern energy technologies from petroleum geology to geological carbon sequestration and radioactive waste management. However, despite their utility and ubiquity, many of their properties remain poorly understood. In particular, the ability to predict the permeability and mechanics of these media remains a persistent fundamental challenge in the geosciences. In the present work, we show how large-scale classical molecular dynamics (MD) simulations can help interpret the properties of fine-grained sedimentary material. All-atom simulations containing 30 discrete clay particles are utilized to understand the evolution of a clay nanoparticle suspension during its progressive dehydration. Microstructural (pore size distribution, tortuosity, anisotropy), thermodynamic (enthalpy and free energy of hydration, anion exclusion), mechanical (total suction), and transport properties (diffusion coefficient tensors of water and sodium) are calculated and compared to the experiment. Overall, our results provide new insight into the coupled chemistry, mechanics, and transport properties of disordered nanoparticle assemblages and shed light upon the important role of water films in controlling these properties.

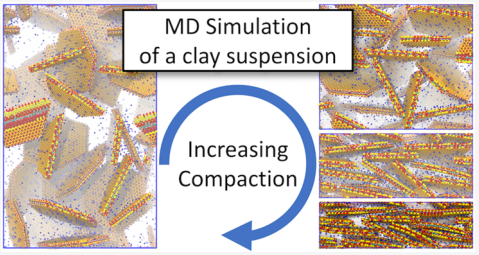

INTRODUCTION

Nanoporous assemblages of water and clay minerals are one of the hallmarks of terrestrial weathering and sedimentary environments.[1,2] They occur ubiquitously as flocs, gels, aggregates, and surface coatings in soils and coarse-grained sedimentary rocks such as sandstones[3−5] and, also, as load-bearing phases in fine-grained sedimentary media such as shales and mudstones,[6,7] formations that account for ∼70% of the world's sedimentary rock mass.[8−10]

Due to their large surface area to volume ratio and high cation-exchange capacity, clay minerals tend to dictate the properties of rocks and soils, particularly when the total clay fraction contains a significant proportion of swelling clay minerals, i.e., smectites.[4,11] As a result, fundamental processes at clay−water interfaces have important ramifications for humanity's food security (through their impacts on soil formation and soil health)[12−14] and for the Earth's carbon cycle (as illustrated by the existence of well-established but poorly understood correlations between smectite clay and organic carbon content in both soils and sediments).[15,16] In addition, clay minerals play a vital role in two low-carbon energy technologies: carbon capture and storage (CCS) and nuclear waste management that rely on the sealing properties of clay-rich rocks for the long-term geologic storage of supercritical CO_2 and high-level radioactive waste.[17−23] The applications noted above highlight the need for a deep fundamental understanding of the ability of clay minerals to influence flow, mechanics, and chemistry in the subsurface.[11,24−27]

A recurrent theme in studies of the impact of clay minerals on the properties of soils and sedimentary rocks is the expectation that the macroscale properties of these media can be linked, more-or-less directly, to the nanoscale properties of clay−water assemblages.[28−30] The existence of such a link is indicated by the extensive evidence that changes in the solid−water ratio of these assemblages at the nanoscale have a strong influence on the macroscale properties of argillaceous media. One example of this is the pronounced threshold in the core-scale permeability and mechanics of fine-grained sedimentary rocks at a clay mineral mass fraction of ∼1/3 where the nanoporous clay becomes load-bearing.[6,11,30−32] Another example is the strong influence of salinity-driven changes in clay aggregation at the nanoscale on the sedimentation, rheology, swelling pressure, and transport properties of clay−water mixtures at the macroscale.[33−37]

Efforts to characterize the nanoscale structure, energetics, and transport properties of clay−water assemblages are notoriously arduous, in part because these assemblages are stabilized by relatively weak interparticle interactions across nanometer-scale water films.[29,38,39] These interactions are highly sensitive to changes in the hydration state, external confining pressure, and aqueous chemistry conditions including salinity[40] and connate counterion identity.[41] Experimental techniques that provide a nanoscale view of minimally disrupted smectite−water

Received: December 2, 2019
Revised: January 20, 2020
Published: January 21, 2020

https://dx.doi.org/10.1021/acs.jpcc.9b11197
J. Phys. Chem. C 2020, 124, 3702−3714

assemblages [predominantly X-ray diffraction (XRD),[40,42,43] small-angle X-ray scattering (SAXS),[44−47] and cryogenic transmission electron microscopy (cryo-TEM)[46,48,49]] indicate that they generally consist of relatively complex microstructures involving the coexistence of several stable hydration states, including crystalline hydrates with interclay separations of 0.3, 0.6, or 0.9 nm and osmotic hydrates with interclay separations of ≥3 nm. The crystalline hydrates are thought to be controlled by short-range ion and surface hydration forces in discrete water layers sandwiched between adjacent clay basal surfaces, whereas the osmotic hydrates are thought to reflect a balance of long-range van der Waals and electrostatic interactions between clay nanoparticles.[49−52] To date, no model has successfully incorporated both osmotic and crystalline hydrates simultaneously to correctly describe the structure, hydraulic permeability, or other properties of hydrated clay assemblages.

One promising approach to describe the complex structure and transport properties of fine-grained sedimentary rocks is computational modeling.[24] At the microscale, Monte Carlo or Brownian dynamics simulations of several thousand cylindrical disks have helped elucidate the role of compaction and particle size anisotropy on the porosity and structural ordering of fine-grained sedimentary media.[53−55] Such models, however, typically use simple hard-disk or mean-field Poisson−Boltzmann potentials, neither of which can explain the concomitant existence of crystalline and osmotic hydrates found within the clay matrix. At the nanoscale, molecular dynamics (MD) simulations have helped to validate many of the experimental observations on the hydration and transport properties of clay minerals.[56−58] Molecular dynamics simulations, in particular, have been very successful in describing, for example, the structure of crystalline hydrates corresponding to discrete mono-, bi-, and trilayers of water molecules between adjacent clay surfaces,[59−61] the structure of the electrical double layer (EDL) formed at the surface of the charged clay mineral,[58,62,63] and the transport (diffusion in particular) of water and ions in individual clay interlayer nanopores.[64−67]

While previous MD simulations have been quantifiably successful in a variety of metrics, they have almost exclusively been limited to examining idealized infinite clay lamellae. This is primarily due to the immature parametrization of the edge site structures of the clay minerals[68,69] but also due to the previously unavailable computational resources required to perform a simulation of the clay matrix with an all-atom resolution. Consequently, many significant structural and transport properties have been impossible to calculate. For example, previous simulations have not been able to capture hydraulic permeability, anion exclusion, or anion diffusion, which are disproportionately sensitive to the largest pores in the system.[58,70] To calculate such quantities inherently requires a model that can accurately predict both the pore size distribution and the characteristic tortuosity found within hydrated clay assemblages.[71−73]

In the present work, we use large-scale MD simulations to address these issues by modeling an assemblage of 30 nanoparticles of Na-montmorillonite, the prototypical swelling smectite clay, at various states of dehydration. Our aim is to understand the microstructure, mechanics, energetics, and transport properties of hydrated clay as a function of dehydration or compaction. This has, for the first time, been made possible by combining recent methodological advances used to describe the edge structures of clay minerals[68,74−78] in concatenation with newly available large-scale high-performance computing resources.[79,80] All-atom simulations containing many discrete clay particles are utilized to understand the properties of hydrated clay assemblages found within soils and sedimentary media as a function of dry bulk density ρ_b (or porosity ϕ).

While the methodological advances and results of this Article focus on the properties of fine-grained argillaceous media, the overall challenge associated with describing the transport properties and mechanics of soft nanoporous or colloidal materials where both short- and long-range interactions are important is far more general. The methods and results presented in this Article are pertinent to essentially all endeavors that involve hydrated charged nanopores or nanoparticle assemblages including in biology, nanofluidics, nanofiltration, and material sciences.[81−83]

METHODS

Simulation Methodology. The simulation procedures used in this study are described in full detail in the Supporting Information. Briefly, the clay examined was a Na-montmorillonite (the prototypical swelling smectite) with stoichiometry $Na_{0.8}^{+}[Al_{3.2}Mg_{0.8}]Si_8O_{20}(OH)_4$. The initial structure was based on that of pyrophyllite-1Tc.[84] Isomorphic substitutions of Al^{3+} to Mg^{2+} were randomly placed within the clay sheet such that no two Mg^{2+} substitutions share polyhedral elements with one another.[85] The resulting negative structural charge was balanced with adsorbed Na ions. Idealized systems containing infinite clay lamellae [corresponding to the 0-, 1-, 2-, 3-, and 4-layer crystalline hydrates as well as a stable osmotic hydrate (6 nm-wide nanopore)] were generated by creating infinitely periodic clay sheets with dimensions of 42 Å × 45 Å in the *xy* plane (i.e., 8 × 5 unit cells), hydrating the interlayer nanopores with an appropriate water content,[59,64] and replicating the system in *z* such that the MD simulation cell was at least 40 Å in the *z*-direction (Figure S1).

Disordered systems containing 30 randomly oriented hexagonal clay lamellae were prepared by cleaving a pyrophyllite slab along two [010] and four [110] edges (the so-called AC and B edges of White and Zelazny)[75,86] to create a hexagonal particle with a minor diameter of 10 nm; healing the resulting edges as per White and Zelazny at near neutral pH; distributing isomorphic substitutions and charge-compensating Na^+ ions as described above. An example clay particle generated using this procedure is presented in Figure S2, and the process used to generate the clay edges is presented in Figure S3. Hexagonal particles were generated and added sequentially with a random position and orientation within a 24 × 24 × 40 nm^3 simulation cell, such that no two clay particles overlap, until 30 particles were successfully placed. To minimize unintended orientational correlations, 300 separate unique configurations of the 30 particles were generated. For each configuration, we calculated the widely used scalar order parameter *S*,[53,87] which quantifies the amount of orientational correlations between particles as described in the Supporting Information. This order parameter corresponds directly to the average of the second-order Legendre polynomial ($\langle P_2 \rangle$) frequently accessed experimentally via XRD analyses. A completely isotropic sample of clay particles would have $S = 0$, while perfectly ordered clay particles would have $S = 1$. Liquid crystals, for example, typically have $S \approx 0.5$ to 0.8. From the 300 unique initial configurations, we chose the most randomly oriented ($S \approx 0.1$) as the starting configuration to examine the behavior of Na-montmorillonite under compaction (Figure S4). Finally, the selected configuration of

https://dx.doi.org/10.1021/acs.jpcc.9b11197
J. Phys. Chem. C 2020, 124, 3702−3714

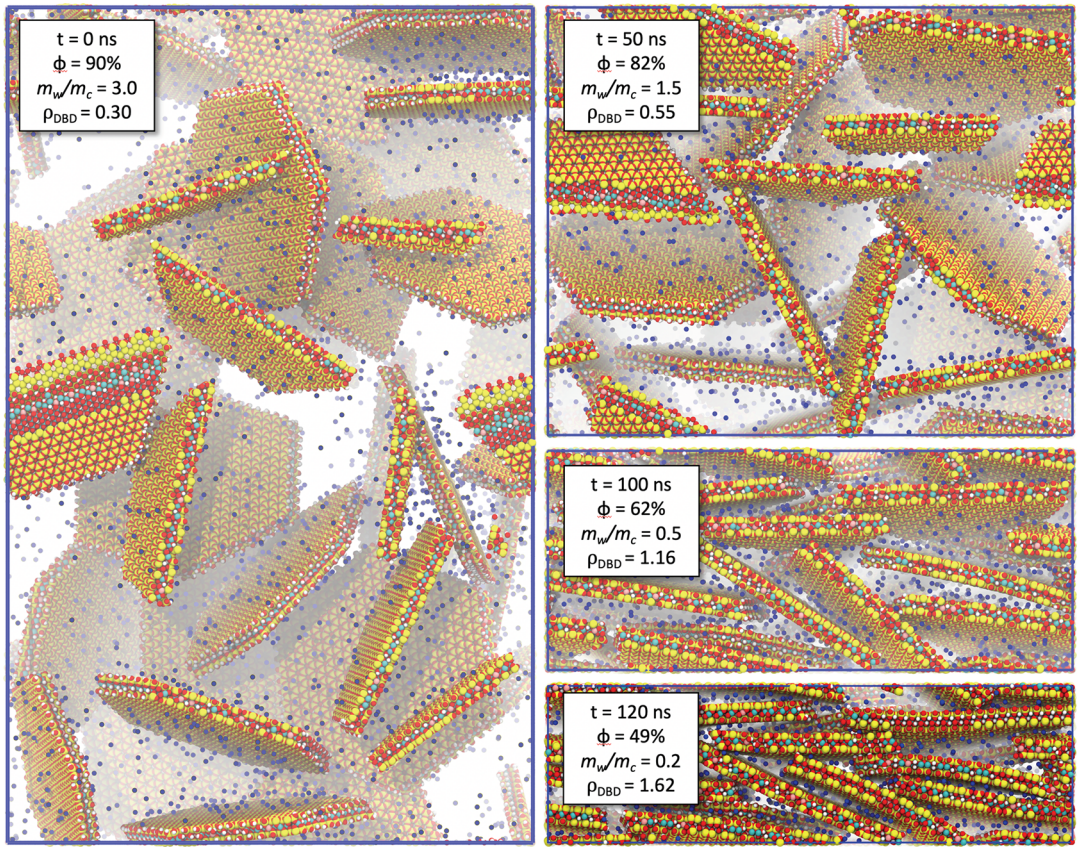

Figure 1. Snapshots of configurations predicted via MD simulation during the dehydration of a Na-montmorillonite suspension (water molecules not shown). The initial configuration (left) had minimal orientational correlations between clay particles, while the final structures present stacking features and correlations representative of the clay matrix.

clay particles was solvated using about 660 000 water molecules, resulting in a system containing over 2.4 million atoms in total with a water to clay mass ratio (m_W/m_C) of ≈3. A snapshot of the starting configuration is presented on the left of Figure 1.

Molecular dynamics (MD) simulations were performed using the GROMACS 2016.3 software package.[88] The simulations used periodic boundary conditions with a real space (van der Waals and electrostatic) cutoff of 12 Å, with long-ranged electrostatics calculated using the particle−particle−particle−mesh Ewald summation method with an accuracy of 99.95%. Interatomic interactions were described using the ClayFF model for clay atoms,[89] the SPC/E water model,[90] and the Smith−Dang parametrization for Na^+ ions.[91] To model clay edge atoms, we follow the procedure introduced by Lammers et al.[74] as illustrated in Figure S3. An overview of the interaction potentials used in this study can be found in the Supporting Information. Throughout all simulations, bonds involving a H atom (within both clay and water) were restrained using the LINCS algorithm, while the geometry of each water molecule was further restrained using the SHAKE algorithm.

All simulations were initialized with an energy minimization procedure to minimize any unphysical overlap between nearby atoms. The minimized structures were then equilibrated for 100 ps in the NVT ensemble at 298 K as described in the Supporting Information. Further equilibration simulations were then performed in the NPT or NP_zT ensembles (for systems containing periodic basal clay sheets or multiple hexagonal clay particles, respectively) at 298 K and 101.325 kPa for 10 ns. Production simulations were then performed in the same isobaric−isothermal ensemble at 298 K and 101.325 kPa. For the idealized systems of periodic Na-montmorillonite, production MD simulations were carried out for 10 ns; analyses of these systems were carried out over the final 5 ns of the production simulation for each hydration state.

To reproduce the compaction of Na-montmorillonite, the system containing discrete hexagonal clay particles was simulated for 1 ns, after which a select number of water molecules was randomly deleted from the system. This process was repeated until all water molecules were removed from the system. Initially, we removed 6600 water molecules from the system every 1 ns. Once the system reached a water to clay mass ratio of 1, the dehydration rate was halved, a procedure that was found to help reduce stacking defects in the simulation. We note that a constant chemical potential simulation may be preferable to this process; however, this approach is currently computationally untenable for systems of the considered size.

Overall, the dehydration process took over 134 ns to complete, excluding the additional 10 ns utilized to initially equilibrate the system. Visual inspection of the resulting structures suggests that the dehydration process was carried out sufficiently slowly to allow the particles to orient and form structures similar to those expected under real-world dehydration,[42,92] as presented in the right-hand panel of Figure 1 and the video in the Supporting Information. Analyses of the disordered systems were carried out using the final 0.5 ns of each 1 ns dehydration step.

Data Analyses. Data analysis procedures are described in detail in the Supporting Information. Briefly, porosity was

https://dx.doi.org/10.1021/acs.jpcc.9b11197
J. Phys. Chem. C 2020, 124, 3702−3714

calculated using two techniques. The first quantifies the expected volume fraction occupied by pore water (ϕ_1), i.e., the number of water molecules in the system multiplied by the molecular volume of bulk liquid water at standard temperature and pressure divided by the total volume of the simulation cell. The second quantifies the volume fraction not occupied by the solid (ϕ_2), determined by carrying out a hard-sphere test-particle insertion (TPI) calculation with appropriate hard-sphere radii assigned to clay atoms and recording the ratio of successful to total insertion attempts of a hard-sphere with radius r = 0 nm.

The pore-size distribution (PSD) of the clay matrix at each stage of compaction was characterized using two metrics. The first metric (PSD_1) is based on the distance of any location in the pore space to the nearest clay surface[93−95] determined using hard-sphere TPI calculations with particles of varying radii. The resulting PSD can be manipulated to obtain properties such as the solvent-accessible solvent area (SASA, i.e., the Connolly surface of water about the clay particles[95]) and the pore volume fraction associated with successive hydration layers of water surrounding the clay minerals. The second metric (PSD_2) is based on the average distance of any water molecule to the two nearest clay surfaces. For slit-shaped pores, this metric enables one to identify the fraction of water molecules located in different types of crystalline hydrates. With minor manipulation, it also enables one to identify water molecules that are interfacial but not contributing to crystalline hydrates.

Enthalpies of hydration were calculated from the predicted total potential energy (U) of the simulated systems in units of kJ/kg$_c$ (energy per mass of clay) using relations described in the Supporting Information. These relations were used to calculate the differential enthalpy of hydration of our simulated systems ($\Delta h_{hydration}$)[96] as a function of water content (i.e., the enthalpy associated with the addition of a single water molecule to the system) and, also, the overall heat released by immersing a clay sample of known prehydration state into a reservoir of bulk liquid water (ΔQ).

The excess chemical potential of water ($\mu_{w,\,excess}$) at each stage of dehydration was calculated using the Widom test-particle insertion technique.[87,97] In our simulated systems, this excess chemical potential equals the Gibbs free energy associated with the addition of a single water molecule to the system ($\Delta g_{hydration}$). The contribution of entropic phenomena to the differential free energy of hydration, $-T\Delta s_{hydration}$, was calculated as the difference between $\Delta g_{hydration}$ and $\Delta h_{hydration}$. In addition, the difference between the excess chemical potentials of water in the clay pore space and in a reference state of bulk liquid water at identical T and P ($\Delta\mu_w$) was used to calculate the activity of water [$a = \exp(\Delta\mu_w/kT)$] and the total suction of the simulated systems [$P_s = -\Delta\mu_w/\overline{v}_w$, where $\overline{v}_w$ is the partial molar volume of bulk liquid water].[96,98−101]

Finally, the diffusion coefficients of water molecules and Na^+ ions were calculated from the mean-squared displacement of each species using the Einstein relation.[87,102] An apparent tortuosity tensor of the disordered system was subsequently calculated by comparing the diffusion coefficients in the disordered system (D_{ii}) to a weighted sum of diffusion coefficients parallel to the clay surface in the ordered n-layer hydrates of montmorillonite (D_{ii}^n): $\tau_{ii} = (\Sigma_n D_{ii}^n f^n)/D_{ii}$, where f^n represents the fraction of all water or sodium ions forming n-layer hydrates calculated using the PSD_2 metric introduced above and the diffusion coefficients in crystalline hydrates were taken from Holmboe and Bourg.[64]

RESULTS AND DISCUSSION

Porosity. The porosity of the clay matrix as calculated using both methods outlined above is presented in Figure 2a. Porosity values calculated using the hard-sphere TPI method decrease

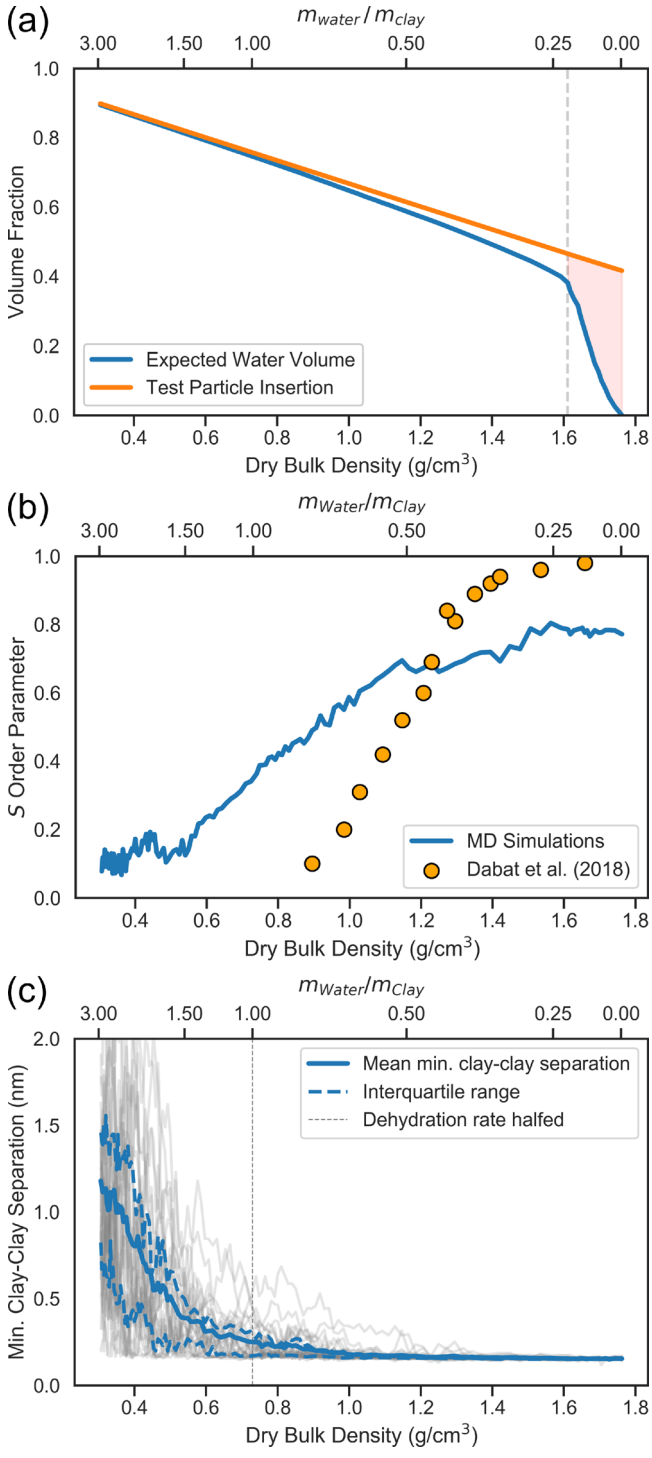

Figure 2. (a) Porosity of the disordered clay−water system as a function of ρ_b as quantified using two different methods. (b) S order parameter as a function of ρ_b (blue curve). The orange circles show predictions based on large-scale simulations of hard disks.[53] (c) Minimum clay−clay interparticle separation for every particle in the system, plotted as a function of ρ_b (gray lines) along with the mean, lower, and upper quartiles (blue lines).

https://dx.doi.org/10.1021/acs.jpcc.9b11197
J. Phys. Chem. C 2020, 124, 3702−3714

linearly with ρ_b, indicating that the density of the clay particles is invariant with dehydration. Values calculated by the expected water method show marginal variance from the TPI values at $\rho_b \leq 1.6$ g/cm^3 with minor nonlinearity indicating that the average density of pore water decreases with decreasing water content. This finding is consistent with previous MD simulations of infinitely periodic clay systems, which show that, while water in ideal crystalline hydrates has a density close to that of bulk liquid water, systems with transitional interlayer spacings (e.g., in a 1.5-layer hydrate) present a significantly lower density of interlayer water.[64] This suggests that there is likely suboptimal packing of water in our dehydrating clay system as we frequently observe the coexistence of different hydration states within the same interlayer.

An important feature highlighted by Figure 2a is the deviation in calculated porosities at $\rho_b \approx 1.6$ g/cm^3. At this point in the simulation, the system volume becomes relatively invariant with water content (Figure S5). This point corresponds to a phase separation of the water molecules in the simulation into a liquid phase sorbed to the solid surfaces and a vapor phase existing within mesopores associated predominantly with stacking defects. As will be shown later on, this formation of water vapor coincides with a decrease in the activity of water and a large increase in total suction.

Order Parameter *S*. Figure 2b presents the variation in the *S* order parameter as a function of ρ_b. Also presented in Figure 2b is the data set produced by Dabat et al.[53] using particle scale simulations of hard disks of similar aspect ratio to our clay particles. As noted by Dabat et al., their prediction agrees with the experimental data obtained by gravity-driven compaction of millimeter-scale polytetrafluoroethylene disks. In comparison to the larger-scale results, our MD simulations tend to overestimate the *S* order parameter at low ρ_b values and underestimate this parameter at high ρ_b values. These deviations are consistent with the expectation that our small system size (only 30 particles vs 5500 in the work of Dabat et al.) should tend to inhibit disorder in dilute systems while inhibiting order in dense systems. In addition, the difference in *S* at low ρ_b values may reflect ordering by the long-range interactions between charged clay particles, which are absent in the case of the hard-disk interaction potentials used by Dabat et al.

Finally, we note that we observe three plateaus in our prediction of *S* vs ρ_b. The first plateau occurs at $\rho_b \leq 0.5$ g/cm^3, where $S \approx 0.1$; its end coincides with the lowest dry bulk density at which essentially all clay particles are in direct contact with their nearest neighbor (Figure 2c), suggesting that steric repulsion between clay particles plays an important role in inducing ordering during dehydration. The second plateau occurs at $\rho_b \approx 1.1$ to 1.4 g/cm^3, where $S \approx 0.7$. Finally, the third plateau occurs at $\rho_b \geq 1.6$ g/cm^3, where $S \approx 0.8$; its onset slightly precedes the formation of vapor bubbles (Figure 2a) and coincides with the dry bulk density where steric interactions between clay particles strongly inhibit further reduction in the overall volume of the simulation cell. Notably, the final value of our *S* order parameter agrees remarkably well with the experimentally observed value ($S \approx 0.7$) for thin oriented films of Na-montmorillonite prepared by drying a dilute suspension of clay by Carrier et al.[103]

PSD Method 1. The pore size distribution PSD_1 (i.e., the distribution of distances to the nearest clay surface) is presented at four different ρ_b values in Figure 3. The curves are derived from hard-sphere TPI predictions with probe spheres of different radii shown in Figure S6. Predicted PSD_1 curves are

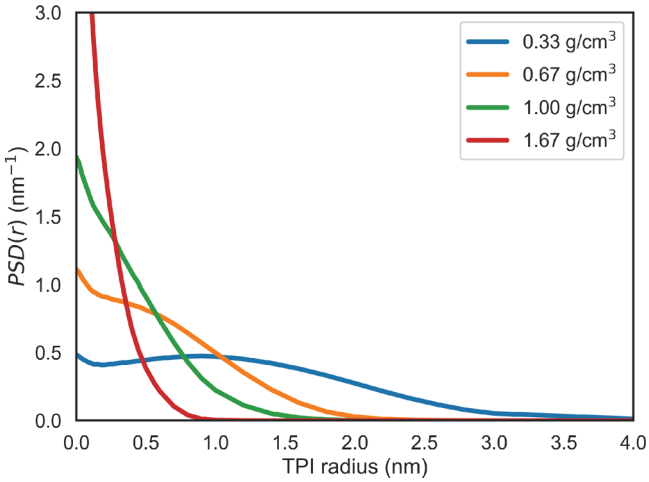

Figure 3. Pore size distribution PSD_1 of the disordered clay system at four ρ_b values.

nonmonotonic at ρ_b 0.5 g/cm^{-3} but become monotonic at higher dry bulk densities. This transition coincides with the dry bulk density where essentially all particles achieve direct contact with their nearest neighbor (Figure 2c). The slight systematic increase in the PSD at TPI probe radii <0.15 nm indicates that the TPI calculation detects small cavities within the clay structure or at the clay−water interface (e.g., ditrigonal cavities of the siloxane surface) that are too small to be accessed by hydrating water molecules. Using this technique, we observe a simultaneous, and approximately equal, increase in the pores available to form all types of crystalline hydrates up to a dry bulk density of 1.2 g/cm^3 and a water-to-clay mass ratio of approximately 0.50 (Figure S8).

For a TPI probe radius of 0 nm, the PSD_1 metric yields the solvent accessible surface area (SASA) as described in the Supporting Information. Calculations of this property yield a SASA of approximately 1300 m^2/g at $\rho_b < 1.4$ g/cm^3, with a small decrease at higher ρ_b values (Figure S7). For comparison, the theoretical and measured specific surface area associated with montmorillonite basal surfaces equals ≈800 m^2/g, while that associated with clay edge surfaces in our simulations should equal ≈165 m^2/g based on the size and geometry of our particles. In short, the SASA values predicted using the PSD_1 metric overestimate the expected specific surface area of our clay particles by about 35%. This discrepancy likely reflects the contribution to the SASA calculation of the small (subwater-molecule size) cavities and surface roughness features noted above.

PSD Method 2. The pore size distribution PSD_2 (based on the average distance of each water molecule to the two nearest clay surfaces) is presented at four ρ_b values in Figure 4a. Unlike the PSD_1 metric, PSD_2 reveals a structure associated with the crystalline hydrates, such as the bimodal distribution observed at $\rho_b = 1.65$ g/cm^3 in Figure 4a. More broadly, it provides a qualification of the confinement environment of each water molecule in the system (as exemplified in Figure 4b) and, therefore, enables one to quantify the relative amounts of *n*-layer hydrates throughout the dehydration (Figure 4c). Also presented in Figure 4c is the fraction of water molecules located on external surfaces of clay stacks.

Overall, Figure 4a reveals relatively little preference for the formation of perfectly stacked crystalline hydrates. The only clear exception is the evidence that pore widths intermediate

https://dx.doi.org/10.1021/acs.jpcc.9b11197
J. Phys. Chem. C 2020, 124, 3702−3714

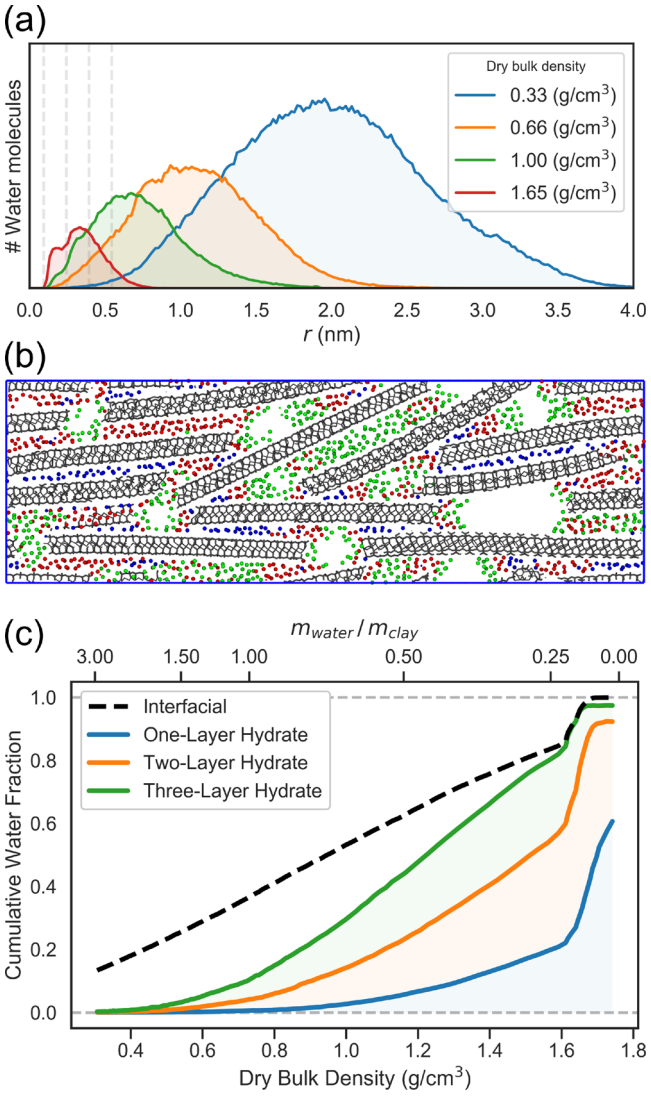

Figure 4. (a) Pore size distribution PSD_2 at four ρ_b values. Vertical dashed lines show the cutoffs used to distinguish the 1-, 2-, and 3-layer hydrates. (b) Snapshot of the system at $\rho_b \approx 1.5$ g/cm^3. Clay particles are shown as gray sticks and water O atoms, as dots color-coded by their chemical environment (1-, 2-, and 3-layer hydrates in blue, red, and green) based on the PSD_2 metric. Water molecules located in mesopores are not shown. (c) Fraction of pore water located in 1-, 2-, and 3-layer hydrates and on external clay surfaces as a function of ρ_b.

between the 0- and 1-layer hydrates and between the 1- and 2-layer hydrates (shown by the first and second vertical dashed lines in Figure 4a) are inhibited. Our results, however, show no evidence of inhibition of pore widths intermediate between the 2- and 3-layer hydrates or between the crystalline and osmotic hydrates. This evidence that energetic barriers to swelling or dehydration are relatively weak beyond the 2-layer hydrate is consistent with MD simulation predictions of the free energy of swelling of a pair of Na-smectite nanoparticles in bulk liquid water.[104]

The results presented above validate various experimental hypotheses based on calorimetric, X-ray diffraction, and gravimetric water sorption experiments regarding the ordering of hydration and dehydration and the coexistence of different hydration environments in smectite films.[42,43,96,105−109] Specifically, our results show that smectite dehydration proceeds through the following sequence of partially overlapping steps: first, the shrinking of large pores concurrently with an increase in particle stacking; second, the drainage of water films located on the external surfaces of clay stacks; third, the drainage of the remaining mesopores associated with the stacking defects; finally, the dehydration of crystalline hydrates proceeding roughly from 3- to 2- to 1-layer hydrates but with extensive coexistence of these species.

Anion Exclusion. For an infinitely thick water film with ionic strength I (in mol/dm^3) on a uniformly charged flat solid surface, the Gouy−Chapman model of the EDL predicts a negative adsorption of co-ions characterized by an average exclusion thickness $d_{ex} = 2 \times \kappa^{-1}$, where κ^{-1} is the Debye length.[110] At 298 K, κ^{-1} is proportional to the inverse square root of I with a proportionality constant equal to 0.304 nm (mol/dm^3)$^{0.5}$. Figure 5 presents a prediction of the resulting anion-

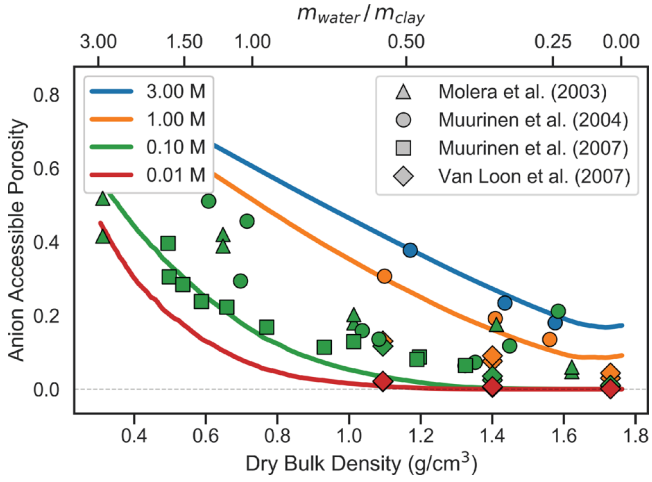

Figure 5. Anion-accessible porosity of compacted Na-smectite as a function of dry bulk density at four ionic strengths. Solid lines were predicted from our MD simulation results using the PSD_1 metric and an average anion-exclusion distance equal to $2\kappa^{-1}$. Symbols show experimental measurements compiled by Tournassat and Appelo[70] from previous studies.[111−114]

accessible porosity approximated as the fraction of the simulation volume located more than $2\kappa^{-1}$ from the nearest clay surface. Although this calculation oversimplifies anion exclusion in clay−water systems (in particular, by using clay microstructural arrangements generated at zero salinity to predict anion exclusion at salinities up to 3 M), it agrees remarkably well with the experimental results on the anion accessible porosity measured using Cl^- or I^- in compacted Na-smectite over a range of salinity conditions. This agreement provides some confidence into the ability of our simulation methodology to predict the pore size distribution of smectite−water assemblages. Also presented in the Supporting Information is the anion accessible porosity at fixed ρ_b for various salt concentrations (Figure S9).

Enthalpy of Hydration. Molecular dynamics simulation predictions of the enthalpy of hydration of our simulated systems are presented in Figure 6 as calculated from the total potential energies of the simulated systems (Figure S10). Specifically, Figure 6a compares values of $\Delta h_{hydration}$ predicted for the disordered clay system with the experimental calorimetry data.[115] At high water contents, the predicted $\Delta h_{hydration}$ value equals −39.39 kJ/mol, in close agreement with experimental (−40.66 kJ/mol) and predicted specific enthalpies of bulk liquid

https://dx.doi.org/10.1021/acs.jpcc.9b11197
J. Phys. Chem. C 2020, 124, 3702−3714

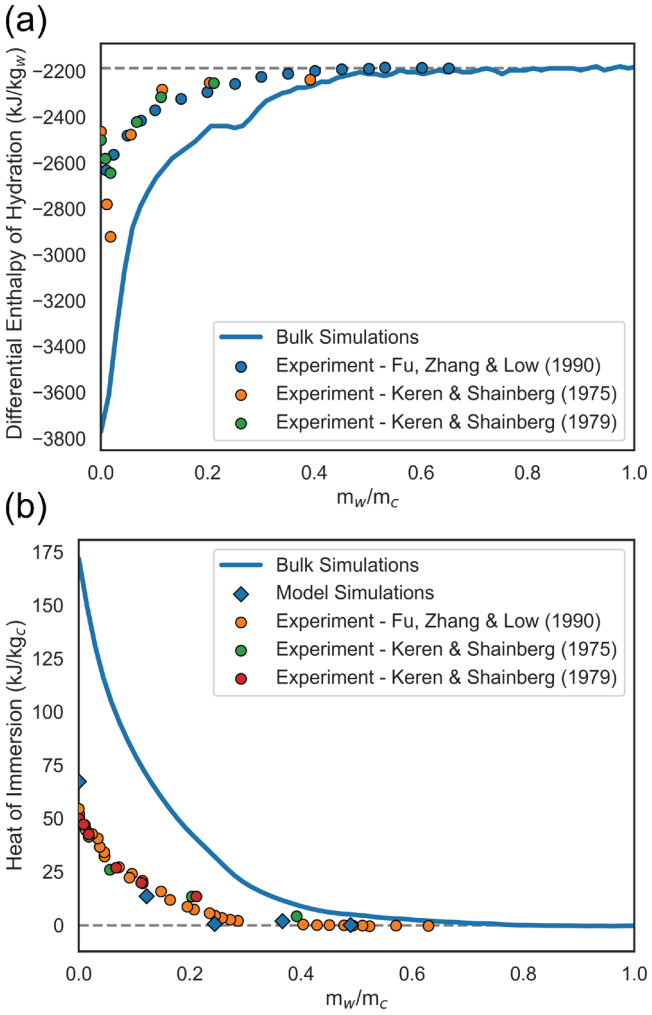

Figure 6. (a) Differential enthalpy of hydration of Na-smectite as a function of m_w/m_c. (b) Integral heat of immersion of clay samples prehydrated to various m_w/m_c values. Experimental data points are measured using immersion calorimetry.

water (−41.4 kJ/mol with the SPC/E water model).[90] At m_w/m_c values below 0.5 (i.e., an average pore width of below ∼1.2 nm), $\Delta h_{hydration}$ deviates from the bulk liquid water value in both simulations and experiments. In short, water located less than 0.6 nm (two monolayers) away from a clay surface is more enthalpically bound to the clay matrix. Notably, we observe that the MD simulations of disordered systems overestimate $\Delta h_{hydration}$ by a factor of 2 relative to the experimental data.

The same results are displayed in Figure 6b as the integral heat of immersion ΔQ of Na-montmorillonite prehydrated to various m_w/m_c values. In Figure 6b, we also present predictions obtained from our simulations of ideally (infinitely periodic) clay particles. The results show that the heat of immersion of dry Na-montmorillonite equals approximately 170 kJ/kg$_c$ in our disordered clay system, 67 kJ/kg$_c$ in our system with ideal periodic basal surfaces, and between 50 and 55 kJ/kg$_c$ in the experiments of Fu et al.[115] and Keren and Shainberg.[116] In short, we observe remarkable agreement between the experimental observations and our simulations of ideal periodic systems, whereas the simulations of disordered systems greatly overestimate the heat of immersion.

For comparison with the ΔQ values of the dry Na-montmorillonite reported above, the value expected for our simulations based only on the hydration enthalpy of exchangeable Na^+ ions is approximately 450 kJ/kg$_c$. This value suggest that the heat of immersion of dry Na-montmorillonite reflects a difference between a large exothermic process (hydration of exchangeable Na^+ ions) and at least one endothermic process (likely including a hydration-induced weakening of clay−clay van der Waals and clay−Na^+ Coulomb attraction) that absorbs 85% of the heat generated by the hydration of Na^+ ions in the simulations of idealized systems but only 62% in the disordered system. The difference in ΔQ values predicted in our simulations of ideal periodic systems vs disordered clay systems is consistent with these endothermic processes being roughly 20% weaker in the disordered systems, in qualitative agreement with the expectation that stacking disorder should cause weaker clay−clay and clay−cation interactions.

Water Excess Chemical Potential. Simulation predictions of water chemical potential as a function of ρ_b are presented in Figure 7a. Predicted values of the chemical potential display noise much larger than the order of k_BT as is frequently observed for the Widom TPI technique. Unfortunately, alternative methods of calculation such as thermodynamic integration or

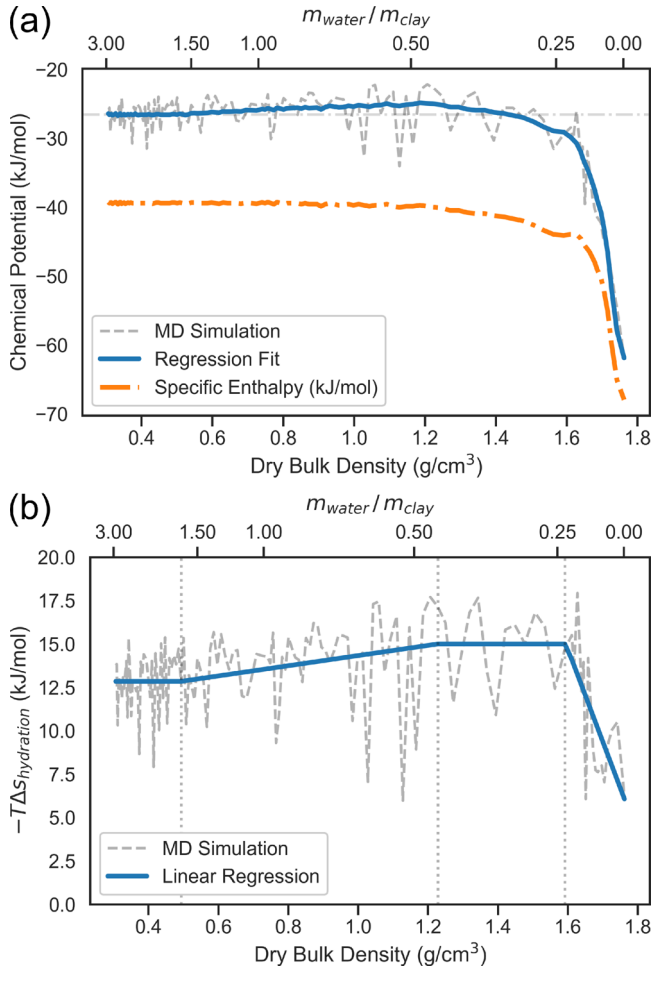

Figure 7. (a) Water excess chemical potential in the disordered clay system as a function of ρ_b. The direct output of the analysis is shown as a gray line. The version smoothed as explained in the text is shown as a blue line. The orange line shows the differential enthalpy of hydration replotted from Figure 6a. (b) Entropic contribution to the differential free energy of hydration.

https://dx.doi.org/10.1021/acs.jpcc.9b11197
J. Phys. Chem. C 2020, 124, 3702−3714

umbrella sampling would be impractical as the simulated system contains many unique and different chemical environments within the same trajectory.

The chemical potential shown in Figure 7a essentially quantifies the differential Gibbs free energy of hydration of the simulated system at a given water content. For comparison, the differential enthalpy of hydration is replotted in Figure 7a as a function of ρ_b. Finally, the entropic contribution to $\Delta h_{hydration}$ (i.e., the difference between the differential free energies and enthalpies shown in Figure 7a) is reported in Figure 7b.

The results presented in Figure 7 reveal different trends depending on ρ_b. For $\rho_b < 0.5$ g/cm^3, the thermodynamics of water uptake in the simulated system is similar to that expected for bulk SPC/E water. From $\rho_b \approx 0.5$ to 1.2 g/cm^3, the entropic contribution becomes increasingly unfavorable while the enthalpic contribution becomes increasingly (but more slowly) favorable. From $\rho_b \approx 1.2$ to 1.6 g/cm^3, the entropic contribution is essentially invariant with ρ_b while the enthalpic favorability continues to increase but at a faster pace. Finally, for $\rho_b > 1.6$ g/cm^3, both entropic and enthalpic contributions to water uptake become rapidly more favorable.

The large statistical fluctuations in our predicted values of $T\Delta s_{hydration}$ do not allow a precise assessment of the functional form of the relationship between $T\Delta s_{hydration}$ and ρ_b. Therefore, we present in Figure 7b a curve based on a series of discrete linear fits in the ranges of ρ_b values noted above. The resulting smoothed data on $T\Delta s_{hydration}$ were combined with the $\Delta h_{hydration}$ data in Figure 7a to obtain the smoothed fit (labeled *regression fit*) to $\Delta g_{hydration}$ shown in Figure 7a.

Water Activity and Total Suction. Simulation predictions of water activity in our disordered clay system are presented in Figure 8a. Despite the large noise in the calculation of water excess chemical potential noted above, an overall trend is clearly discernible: at $\rho_b < 1.25$ g/cm^3, water activity approximately equals 1 in agreement with experimental data.[99,116] At $\rho_b = 1.25$ to 1.65 g/cm^3, water activity progressively decreases from 1 to near 0. Finally, at $\rho_b > 1.65$ g/cm^3, water activity is close to zero. In short, a gradual decrease in water activity precedes the draining of mesopores that occurs at $\rho_b = 1.65$ g/cm^3. During this gradual decrease in water activity, the simulated system still contains a significant fraction of pore water that is not located in a crystalline hydrate or in direct contact with an external clay surface (Figure 4c). Its nonbulk-liquid-like activity may reflect the fact that this mesopore water becomes increasingly stretched as the system approaches cavitation (in agreement with Figure 2a). The earlier onset of the decrease in water activity in our simulations than in the experimental data[99,116] is consistent with the expectation that this stretching of mesopore water should begin at lower ρ_b values in systems with more stacking disorder.

Simulation predictions of total suction P_s in our disordered clay system are presented in Figure 8b. Similarly to the results in Figure 8a, the predictions reveal the existence of three different regimes. At $\rho_b < 1.25$ g/cm^3, $P_s \approx 0$; i.e., water is bulk-liquid-like. At $\rho_b = 1.25$ to 1.65 g/cm^3, it becomes increasingly positive with decreasing water content, in agreement with experimental observations.[106] Finally, at $\rho_b > 1.65$ g/cm^3, we predict very large total suctions consistent with the nucleation of vapor bubbles in the simulated system. For comparison with the values shown in Figure 8b, the Young−Laplace equation (r, where $2\gamma = 72.8$ mN/m is the surface tension of pure liquid water at 298 K) predicts that the total suction in bulk liquid water containing a spherical bubble of vapor with the radius of a single water molecule (0.15 nm) should be on the order of 1000 MPa.

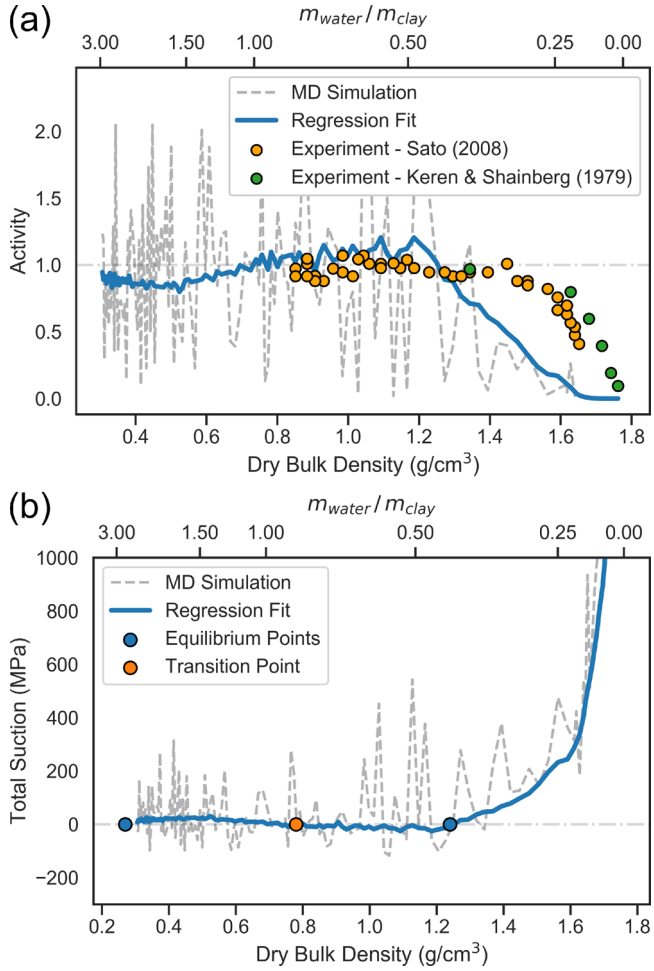

Figure 8. (a) Water activity and (b) total suction in the disordered clay system as a function of dry bulk density. The figures show results calculated from both the direct estimates and smoothed values of water excess chemical potential shown in (a) (dashed and solid lines, respectively) as well as experimental results (circles).[99,116]

A notable feature in Figure 8a is that the activity of water is slightly greater than one at $\rho_b \approx 0.8$ to 1.25 g/cm^3. This prediction is consistent with the observation that interparticle distances between 1 and 2.5 nm (corresponding to ρ_b values between ≈0.8 and 1.4 g/cm^3) are unfavorable based on XRD studies.[40,117] A related observation is the existence of a range of conditions where P_s is slightly negative in Figure 8b. This finding implies that, for $\rho_b \approx 0.3$ to 1.25 g/cm^3, the simulated system should tend to demix into a denser region with $\rho_b = 1.25$ g/cm^3 (i.e., a crystalline hydrate) and a more dilute region with $\rho_b \leq 0.3$ g/cm^3 (i.e., an osmotic hydrate), as observed experimentally.[24]

Water and Sodium Diffusivity. Simulation predictions on the self-diffusion of water are presented in Figure 9. Additional details are presented in the Supporting Information. In particular, the calculation of the slope of the mean-square displacement as a function of time interval τ, reported in Figure S11, indicates that long time scales are required to approach the diffusive limit in the Einstein equation. Results in Figure 9 were calculated using $\tau = 350$ ps. A rough calculation based on the self-diffusion coefficient of bulk liquid water at 298 K shows that the resulting self-diffusion coefficients reflect water diffusion over displacements $(2D\tau)^{0.5} < 1.2$ nm and, therefore, likely underestimate the tortuosity of our simulated systems. The calculation capturing the full tortuosity of our simulated systems

https://dx.doi.org/10.1021/acs.jpcc.9b11197
J. Phys. Chem. C 2020, 124, 3702−3714

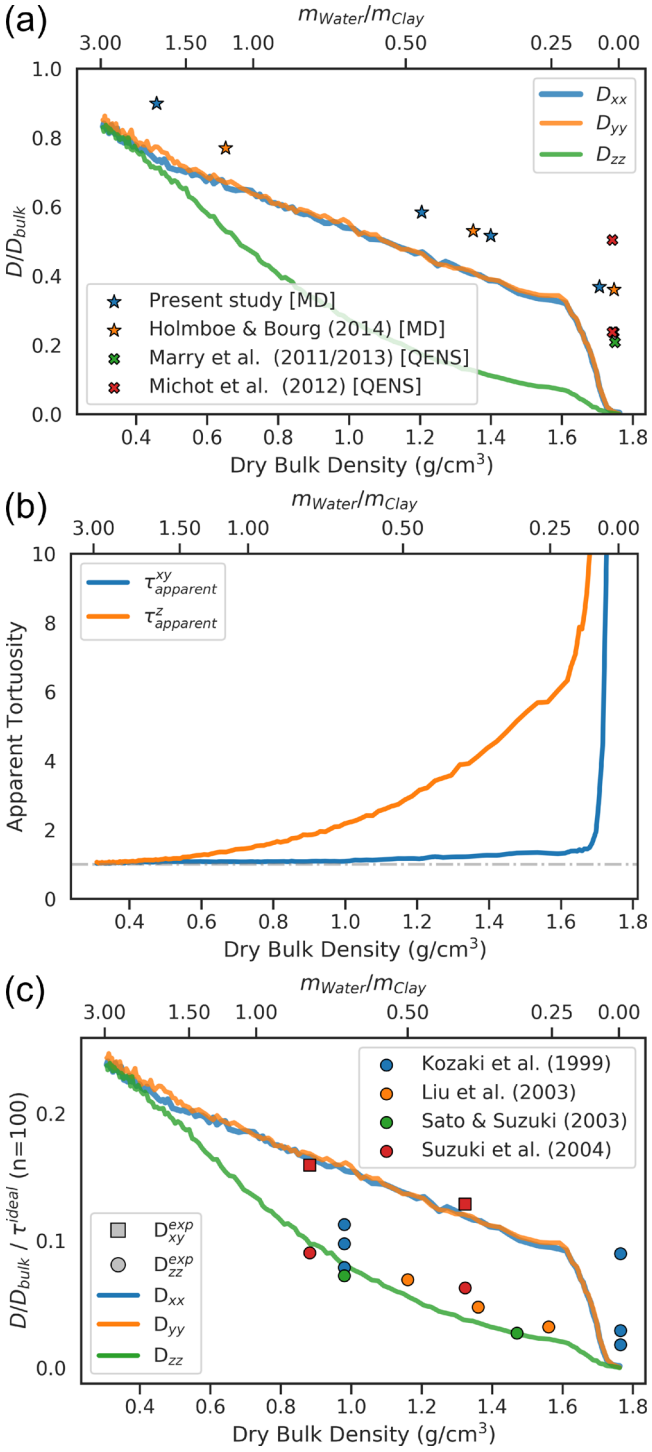

Figure 9. (a) Self-diffusion coefficients of water in the disordered clay system as a function of ρ_b. Symbols show values in individual clay interlayers in the direction parallel to the surface determined by MD simulation (stars)[64] and QENS experiments (crosses).[67,118,119] (b) Apparent tortuosity calculated by comparing the results in (a) to a weighted sum of diffusion coefficients parallel to the surface in idealized nanopores. (c) Results from (a) scaled to match the theoretical tortuosity of an assemblage of disk-shaped platelets with an aspect ratio of 100 at the lowest ρ_b values. Symbols show values measured in cm-scale clay samples in directions perpendicular (squares) or parallel (circles) to compaction.[120−125]

would require the evaluation of the mean-square displacement of water over >35 ns at each hydration state and, hence, a total simulation time >100 times greater than that used in the present study.

Figure 9a shows water self-diffusion coefficients in the *x*, *y*, and *z* direction calculated from the mean-square displacement of water molecules over 350 ps, normalized to the self-diffusion coefficient of bulk SPC/E water (2.615 m^2 s^{-1}, as calculated from a simulation of bulk liquid water). As expected, the simulations predict slower diffusion at higher ρ_b values. At $\rho_b \approx 0.5$ g/cm^3, the simulations predict a splitting in the diffusion coefficients in directions normal and parallel to compaction, i.e., the diffusion coefficient tensor becomes anisotropic. This agrees with the point at which we begin to see an increase in the ordering of the clay particles as quantified by the *S* parameter; it also agrees with experimental measurements on the diffusion coefficient tensor of water in anisotropically compacted Na-smectite samples.[122] The good agreement between diffusion coefficients predicted in the *x* and *y* directions suggest that the simulated system contains a sufficient number of particles that transport properties are not dominated by individual stacking features.

The *xy*-plane diffusion coefficients shown in Figure 9a are broadly consistent with previous results on water diffusion in individual clay interlayer nanopores in the direction parallel to the pore walls as determined using both MD simulations of infinite clay lamellae (stars)[64] and quasi-elastic neutron scattering (QENS) experiments (crosses).[67,118,119] The relatively small offset between diffusion coefficients parallel to the clay surfaces in individual clay interlayers (symbols) and diffusion coefficients in the *xy*-plane in our disordered clay system (blue and orange lines) suggests that the tortuosity of the disordered clay system in the *xy*-plane as sampled over 350 ps intervals is close to 1.

The previous assessment is confirmed by our calculation of the apparent tortuosity of the simulated system obtained by comparing the water self-diffusion coefficient in our disordered system to a weighted sum of water self-diffusion coefficients in ideal systems of *n*-layer hydrates (weighted by the fraction of water in each chemical environment reported in Figure 4c). Our calculation, presented in Figure 9b, shows that the apparent tortuosity in the *xy*-plane is approximately equal to 1 for all ρ_b values. The results in Figure 9b further indicate that the predicted *D* values in Figure 9a underestimate the effect of tortuosity: for the lowest ρ_b values examined here, our calculations predict a tortuosity of ≈1 whereas the theoretical prediction for an assemblage of disk-shaped platelets with an aspect ratio of 10 equals ≈1.12.[126,127]

As a first-order correction for the observation that the self-diffusion coefficients in Figure 9a underestimate the tortuosity of the simulated systems, we scaled these diffusion coefficients by the theoretical prediction of Fricke for an isotropic suspension of disks with an aspect ratio of 100 (roughly representative of real Na-smectite particles)[128] at the lowest ρ_b value in Figure 9b in order to compare our simulation predictions with macroscopic-scale measurements of water self-diffusion in anisotropically compacted, water-saturated Na-smectite samples.[126,127] The results, presented in Figure 9c, show a remarkably good agreement with the experimental data, suggesting that water *D* values measured at the macroscopic scale may be predicted on the basis of three contributions: a nanoscale constrictivity factor that can be accurately evaluated using a weighted sum of self-diffusion coefficients in individual nanopores; an anisotropy to the tortuosity factor that can be evaluated using mean-square displacements sampled over

https://dx.doi.org/10.1021/acs.jpcc.9b11197
J. Phys. Chem. C 2020, 124, 3702−3714

relatively short time intervals in MD simulations of disordered systems; an additional tortuosity factor that can be estimated from theory based on the aspect ratio of the clay nanoparticles. We should note, however, that the agreement shown in Figure 9c could be a fortuitous one (since our MD results are based on a single dehydration simulation) and that further effects are very likely to be important. Notably, the amount of anisotropy that develops during compaction is known to be significantly lower in mixtures of smectite and coarser-grained minerals than in pure smectite,[129,130] such that our use of the Fricke tortuosity model is likely only valid for pure smectite samples. One approach to counteract this would be to upscale the results of this study using random-walk simulations to calculate the macroscopic tortuosity and diffusion in saturated, partially saturated, and non-homogeneous systems as per the work of Churakov, Gimmi, and Tyagi.[66,131,132] We also note that the divergence between experimental and simulated values of water diffusion at high dry bulk densities correspond to conditions where the experimental samples are water saturated and the simulated systems are not (i.e., above a ρ_b of 1.65 g/cm^3 in our simulations).

The self-diffusion coefficients of Na^+ ions, presented in Figure S12, follow a similar trend to that observed for water molecules. In particular, we note a similar split in the self-diffusion coefficients at $\rho_b \approx 0.5$ g/cm^3, with diffusion in the x and y directions broadly identical for all dry bulk densities and greater to that of the self-diffusion coefficient of Na^+ in the z direction. Furthermore, we observe that Na^+ ions diffuse slower compared to water within the same chemical environment and in a system with the same tortuosity, i.e., the ratio $(D^{Na}/D^{Na}_{bulk})/(D^{Water}/D^{Water}_{bulk})$ remains constant at approximately 0.7 for dry bulk densities up to $\rho_b \approx 1.3$ g/cm^3 and gradually decreases to a ratio of 0.3 at $\rho_b \approx 1.65$ g/cm^3. We ascribe this behavior to the different constrictivity observed by a Na^+ ion within the clay matrix compared to a water molecule, in keeping with experimental observations that the surface mobility of adsorbed Na^+ ions in the clay matrix is roughly half of that expected on the basis of their self-diffusion coefficient in bulk liquid water.[71,133,134]

CONCLUDING REMARKS

In this study, we have shown how large-scale MD simulations can be utilized to help interpret many of the microstructural, thermodynamic, mechanical, and transport properties of hydrated clay nanoparticle assemblages. These properties include novel calculations of anion exclusion, pore-size distribution, anisotropy, and tortuosity; enthalpy and free energy of hydration; total suction; diffusion of water and sodium ions. This has been made possible for the first time by combining recent advances used to describe the edge structures of clay minerals along with newly available large-scale high-performance computing resources. Overall, our results indicate that large-scale MD simulations can provide realistic predictions of the properties of hydrated clay nanoparticle assemblages and can shed significant insight into the properties of soft nanoporous or colloidal materials stabilized by interactions across water films, where both short- and long-range interactions are important.

ASSOCIATED CONTENT

Supporting Information

The Supporting Information is available free of charge at https://pubs.acs.org/doi/10.1021/acs.jpcc.9b11197.

Full description of the MD methodology and data analyses as well as further results referenced within the text (PDF)

Video presenting the dehydration of the large assemblage of Na-smectite over a 134 ns time frame and also showing the S order parameter during the simulation (MPG)

AUTHOR INFORMATION

Corresponding Authors

Thomas R. Underwood − *Department of Civil and Environmental Engineering and Princeton Environmental Institute, Princeton University, Princeton, New Jersey 08544, United States;* orcid.org/0000-0001-6323-0055; Email: thomas.underwood@princeton.edu

Ian C. Bourg − *Department of Civil and Environmental Engineering and Princeton Environmental Institute, Princeton University, Princeton, New Jersey 08544, United States;* orcid.org/0000-0002-5265-7229; Email: bourg@princeton.edu

Complete contact information is available at: https://pubs.acs.org/10.1021/acs.jpcc.9b11197

Notes

The authors declare no competing financial interest.

ACKNOWLEDGMENTS

This research was supported primarily by the U.S. Department of Energy, Office of Science, Office of Basic Energy Sciences, Geosciences Program under Award DE-SC0018419. Molecular dynamics simulations were performed using resources of the National Energy Research Scientific Computing Center (NERSC), which is supported by the U.S. Department of Energy, Office of Science, under award DE-AC02-05CH11231. Additional support was provided by Princeton Environmental Institute through its Grand Challenges Program and Carbon Mitigation Initiative.

REFERENCES

(1) Konta, J. Clay and man: clay raw materials in the service of man. *Appl. Clay Sci.* **1995**, *10*, 275−335.

(2) Sposito, G.; Skipper, N. T.; Sutton, R.; Park, S.-h.; Soper, A. K.; Greathouse, J. A. Surface geochemistry of the clay minerals. *Proc. Natl. Acad. Sci. U. S. A.* **1999**, *96*, 3358−3364.

(3) Sposito, G. *The chemistry of soils*; Oxford University Press, 2008.

(4) Nadeau, P. H. An experimental study of the effects of diagenetic clay minerals on reservoir sands. *Clays Clay Miner.* **1998**, *46*, 18−26.

(5) Peters, C. A. Accessibilities of reactive minerals in consolidated sedimentary rock: An imaging study of three sandstones. *Chem. Geol.* **2009**, *265*, 198−208.

(6) Keller, L. M.; Schuetz, P.; Erni, R.; Rossell, M. D.; Lucas, F.; Gasser, P.; Holzer, L. Characterization of multi-scale microstructural features in Opalinus Clay. *Microporous Mesoporous Mater.* **2013**, *170*, 83−94.

(7) Gaboreau, S.; Robinet, J.-C.; Prêt, D. Optimization of pore-network characterization of a compacted clay material by TEM and FIB/SEM imaging. *Microporous Mesoporous Mater.* **2016**, *224*, 116−128.

(8) Yang, Y.; Aplin, A. C. Permeability and petrophysical properties of 30 natural mudstones. *Journal of Geophysical Research: Solid Earth* **2007**, *112*, B03206.

(9) Yang, Y.; Aplin, A. C. A permeability-porosity relationship for mudstones. *Mar. Pet. Geol.* **2010**, *27*, 1692−1697.

(10) Shaw, D. B.; Weaver, C. E. The mineralogical composition of shales. *J. Sediment. Res.* **1965**, *35*, 213−222.

(11) Bourg, I. C. Sealing shales versus brittle shales: a sharp threshold in the material properties and energy technology uses of fine-grained sedimentary rocks. *Environ. Sci. Technol. Lett.* **2015**, *2*, 255−259.
(12) Suarez, D. L. Sodic soil reclamation: Modelling and field study. *Soil Research* **2001**, *39*, 1225−1246.
(13) Calabrese, S.; Richter, D. D.; Porporato, A. The formation of clay-enriched horizons by lessivage. *Geophys. Res. Lett.* **2018**, *45*, 7588−7595.
(14) Maher, K.; Steefel, C. I.; White, A. F.; Stonestrom, D. A. The role of reaction affinity and secondary minerals in regulating chemical weathering rates at the Santa Cruz Soil Chronosequence, California. *Geochim. Cosmochim. Acta* **2009**, *73*, 2804−2831.
(15) Rasmussen, C.; Heckman, K.; Wieder, W. R.; Keiluweit, M.; Lawrence, C. R.; Berhe, A. A.; Blankinship, J. C.; Crow, S. E.; Druhan, J. L.; Pries, C. E. H.; et al. Beyond clay: towards an improved set of variables for predicting soil organic matter content. *Biogeochemistry* **2018**, *137*, 297−306.
(16) Ransom, B.; Kim, D.; Kastner, M.; Wainwright, S. Organic matter preservation on continental slopes: importance of mineralogy and surface area. *Geochim. Cosmochim. Acta* **1998**, *62*, 1329−1345.
(17) Ewing, R. C.; Whittleston, R. A.; Yardley, B. W. Geological disposal of nuclear waste: a primer. *Elements* **2016**, *12*, 233−237.
(18) Madsen, F. Clay mineralogical investigations related to nuclear waste disposal. *Clay Miner.* **1998**, *33*, 109−129.
(19) Delage, P.; Cui, Y.-J.; Tang, A. M. Clays in radioactive waste disposal. *Journal of Rock Mechanics and Geotechnical Engineering* **2010**, *2*, 111−123.
(20) Holloway, S. Storage of fossil fuel-derived carbon dioxide beneath the surface of the earth. *Annual Review of Energy and the Environment* **2001**, *26*, 145−166.
(21) Lackner, K. S. A guide to CO2 sequestration. *Science* **2003**, *300*, 1677−1678.
(22) Benson, S. M.; Orr, F. M. Carbon dioxide capture and storage. *MRS Bull.* **2008**, *33*, 303−305.
(23) Benson, S. M.; Cole, D. R. CO2 sequestration in deep sedimentary formations. *Elements* **2008**, *4*, 325−331.
(24) Bourg, I. C.; Ajo-Franklin, J. B. Clay, water, and salt: controls on the permeability of finegrained sedimentary rocks. *Acc. Chem. Res.* **2017**, *50*, 2067−2074.
(25) Skurtveit, E.; Aker, E.; Soldal, M.; Angeli, M.; Wang, Z. Experimental investigation of CO2 breakthrough and flow mechanisms in shale. *Pet. Geosci.* **2012**, *18*, 3−15.
(26) Zachara, J.; Brantley, S.; Chorover, J.; Ewing, R.; Kerisit, S.; Liu, C.; Perfect, E.; Rother, G.; Stack, A. G. Internal domains of natural porous media revealed: critical locations for transport, storage, and chemical reaction. *Environ. Sci. Technol.* **2016**, *50*, 2811−2829.
(27) Kleber, M.; Eusterhues, K.; Keiluweit, M.; Mikutta, C.; Mikutta, R.; Nico, P. S. *Advances in agronomy*; Elsevier, 2015; Vol. *130*; pp 1−140.
(28) Tessier, D.; Lajudie, A.; Petit, J.-C. Relation between the macroscopic behavior of clays and their microstructural properties. *Appl. Geochem.* **1992**, *7* (Suppl. Issue 1), 151−161.
(29) Espinoza, D. N.; Santamarina, J. C. Clay interaction with liquid and supercritical CO2: The relevance of electrical and capillary forces. *Int. J. Greenhouse Gas Control* **2012**, *10*, 351−362.
(30) Revil, A.; Cathles, L. Permeability of shaly sands. *Water Resour. Res.* **1999**, *35*, 651−662.
(31) Marion, D.; Nur, A.; Yin, H.; Han, D.-H. Compressional velocity and porosity in sand-clay mixtures. *Geophysics* **1992**, *57*, 554−563.
(32) Crawford, B.; Faulkner, D.; Rutter, E. Strength, porosity, and permeability development during hydrostatic and shear loading of synthetic quartz-clay fault gouge. *J. Geophys. Res.* **2008**, *113*, B03207.
(33) Tombácz, E.; Szekeres, M. Colloidal behavior of aqueous montmorillonite suspensions: the specific role of pH in the presence of indifferent electrolytes. *Appl. Clay Sci.* **2004**, *27*, 75−94.
(34) DeCarlo, K. F.; Shokri, N. Salinity effects on cracking morphology and dynamics in 3-D desiccating clays. *Water Resour. Res.* **2014**, *50*, 3052−3072.
(35) Mesri, G.; Olson, R. E. Mechanisms controlling the permeability of clays. *Clays Clay Miner.* **1971**, *19*, 151−158.
(36) Carrillo, F. J.; Bourg, I. C. A Darcy-Brinkman-Biot approach to modeling the hydrology and mechanics of porous media containing macropores and deformable microporous regions. *Water Resour. Res.* **2019**, *55*, No. 8096.
(37) Palomino, A. M.; Santamarina, J. C. Fabric map for kaolinite: effects of pH and ionic concentration on behavior. *Clays Clay Miner.* **2005**, *53*, 211−223.
(38) Güven, N.; Pollastro, R.; Society, C. M. *Clay-water Interface and Its Rheological Implications*; CMS workshop lectures; Clay Minerals Society, 1992.
(39) Hetzel, F.; Tessier, D.; Jaunet, A.-M.; Doner, H. The microstructure of three Na+ smectites: The importance of particle geometry on dehydration and rehydration. *Clays Clay Miner.* **1994**, *42*, 242−248.
(40) Norrish, K. The swelling of montmorillonite. *Discuss. Faraday Soc.* **1954**, *18*, 120−134.
(41) Schramm, L. L.; Kwak, J. C. Interactions in clay suspensions: The distribution of ions in suspension and the influence of tactoid formation. *Colloids Surf.* **1982**, *4*, 43−60.
(42) Wilson, J.; Cuadros, J.; Cressey, G. An in situ time-resolved XRD-PSD investigation into Namontmorillonite interlayer and particle rearrangement during dehydration. *Clays Clay Miner.* **2004**, *52*, 180−191.
(43) Holmboe, M.; Wold, S.; Jonsson, M. Porosity investigation of compacted bentonite using XRD profile modeling. *J. Contam. Hydrol.* **2012**, *128*, 19−32.
(44) Muurinen, A.; Carlsson, T.; Root, A. Bentonite pore distribution based on SAXS, chloride exclusion and NMR studies. *Clay Miner.* **2013**, *48*, 251−266.
(45) Michot, L. J.; Bihannic, I.; Thomas, F.; Lartiges, B. S.; Waldvogel, Y.; Caillet, C.; Thieme, J.; Funari, S. S.; Levitz, P. Coagulation of Na-montmorillonite by inorganic cations at neutral pH. A combined transmission X-ray microscopy, small angle and wide angle X-ray scattering study. *Langmuir* **2013**, *29*, 3500−3510.
(46) Tester, C. C.; Aloni, S.; Gilbert, B.; Banfield, J. F. Short- and Long-Range Attractive Forces That Influence the Structure of Montmorillonite Osmotic Hydrates. *Langmuir* **2016**, *32*, 12039−12046.
(47) Ferrage, E.; Hubert, F.; Baronnet, A.; Grauby, O.; Tertre, E.; Delville, A.; Bihannic, I.; Pret, D.; Michot, L. J.; Levitz, P. Influence of crystal structure defects on the small-angle neutron scattering/diffraction patterns of clay-rich porous media. *J. Appl. Crystallogr.* **2018**, *51*, 1311−1322.
(48) Gilbert, B.; Comolli, L. R.; Tinnacher, R. M.; Kunz, M.; Banfield, J. F. Formation and restacking of disordered smectite osmotic hydrates. *Clays Clay Miner.* **2015**, *63*, 432−442.
(49) Whittaker, M. L.; Lammers, L. N.; Carrero, S.; Gilbert, B.; Banfield, J. F. Ion exchange selectivity in clay is controlled by nanoscale chemical-mechanical coupling. *Proc. Natl. Acad. Sci. U. S. A.* **2019**, *116*, 22052−22057.
(50) Derjaguin, B.; Landau, L. Theory of the stability of strongly charged lyophobic sols and of the adhesion of strongly charged particles in solutions of electrolytes. *Prog. Surf. Sci.* **1993**, *43*, 30−59.
(51) Verwey, E. J. W.; Overbeek, J. T. G.; Overbeek, J. T. G. *Theory of the stability of lyophobic colloids*; Courier Corporation, 1999.
(52) Smalley, M. Electrical theory of clay swelling. *Langmuir* **1994**, *10*, 2884−2891.
(53) Dabat, T.; Mazurier, A.; Hubert, F.; Tertre, E.; Grégoire, B.; Dazas, B.; Ferrage, E. Mesoscale Anisotropy in Porous Media Made of Clay Minerals. A Numerical Study Constrained by Experimental Data. *Materials* **2018**, *11*, 1972.
(54) Ferrage, E.; Hubert, F.; Tertre, E.; Delville, A.; Michot, L. J.; Levitz, P. Modeling the arrangement of particles in natural swelling-clay porous media using three-dimensional packing of elliptic disks. *Phys. Rev. E* **2015**, *91*, No. 062210.
(55) Ebrahimi, D.; Whittle, A. J.; Pellenq, R. J.-M. Effect of polydispersity of clay platelets on the aggregation and mechnical

https://dx.doi.org/10.1021/acs.jpcc.9b11197
J. Phys. Chem. C 2020, 124, 3702−3714

properties of clay at the mesoscale. *Clays Clay Miner.* **2016**, *64*, 425−437.
(56) Rotenberg, B.; Marry, V.; Vuilleumier, R.; Malikova, N.; Simon, C.; Turq, P. Water and ions in clays: Unraveling the interlayer/micropore exchange using molecular dynamics. *Geochim. Cosmochim. Acta* **2007**, *71*, 5089−5101.
(57) Greathouse, J. A.; Refson, K.; Sposito, G. Molecular dynamics simulation of water mobility in magnesium-smectite hydrates. *J. Am. Chem. Soc.* **2000**, *122*, 11459−11464.
(58) Tinnacher, R. M.; Holmboe, M.; Tournassat, C.; Bourg, I. C.; Davis, J. A. Ion adsorption and diffusion in smectite: Molecular, pore, and continuum scale views. *Geochim. Cosmochim. Acta* **2016**, *177*, 130−149.
(59) Teich-McGoldrick, S. L.; Greathouse, J. A.; Jove-Colon, C. F.; Cygan, R. T. Swelling properties of montmorillonite and beidellite clay minerals from molecular simulation: comparison of temperature, interlayer cation, and charge location effects. *J. Phys. Chem. C* **2015**, *119*, 20880−20891.
(60) Hensen, E. J.; Smit, B. Why clays swell. *J. Phys. Chem. B* **2002**, *106*, 12664−12667.
(61) Tambach, T. J.; Hensen, E. J.; Smit, B. Molecular simulations of swelling clay minerals. *J. Phys. Chem. B* **2004**, *108*, 7586−7596.
(62) Bourg, I. C.; Sposito, G. Molecular dynamics simulations of the electrical double layer on smectite surfaces contacting concentrated mixed electrolyte (NaCl−CaCl2) solutions. *J. Colloid Interface Sci.* **2011**, *360*, 701−715.
(63) Bourg, I. C.; Lee, S. S.; Fenter, P.; Tournassat, C. Stern layer structure and energetics at mica-water interfaces. *J. Phys. Chem. C* **2017**, *121*, 9402−9412.
(64) Holmboe, M.; Bourg, I. C. Molecular dynamics simulations of water and sodium diffusion in smectite interlayer nanopores as a function of pore size and temperature. *J. Phys. Chem. C* **2014**, *118*, 1001−1013.
(65) Greathouse, J. A.; Hart, D. B.; Bowers, G. M.; Kirkpatrick, R. J.; Cygan, R. T. Molecular simulation of structure and diffusion at smectite−water interfaces: Using expanded clay interlayers as model nanopores. *J. Phys. Chem. C* **2015**, *119*, 17126−17136.
(66) Churakov, S. V.; Gimmi, T. Up-scaling of molecular diffusion coefficients in clays: A two-step approach. *J. Phys. Chem. C* **2011**, *115*, 6703−6714.
(67) Marry, V.; Dubois, E.; Malikova, N.; Breu, J.; Haussler, W. Anisotropy of water dynamics in clays: Insights from molecular simulations for experimental QENS analysis. *J. Phys. Chem. C* **2013**, *117*, 15106−15115.
(68) Newton, A. G.; Kwon, K. D.; Cheong, D.-K. Edge structure of montmorillonite from atomistic simulations. *Minerals* **2016**, *6*, 25.
(69) Pouvreau, M.; Greathouse, J. A.; Cygan, R. T.; Kalinichev, A. G. Structure of hydrated kaolinite edge surfaces: DFT results and further development of the ClayFF classical force field with metal−O−H angle bending terms. *J. Phys. Chem. C* **2019**, *123*, 11628−11638.
(70) Tournassat, C.; Appelo, C. Modelling approaches for anion-exclusion in compacted Nabentonite. *Geochim. Cosmochim. Acta* **2011**, *75*, 3698−3710.
(71) Bourg, I. C.; Sposito, G. Connecting the molecular scale to the continuum scale for diffusion processes in smectite-rich porous media. *Environ. Sci. Technol.* **2010**, *44*, 2085−2091.
(72) Tournassat, C.; Steefel, C. I. Reactive transport modeling of coupled processes in nanoporous media. *Rev. Mineral. Geochem.* **2019**, *85*, 75−109.
(73) Bacle, P.; Dufreche, J.-F.; Rotenberg, B.; Bourg, I. C.; Marry, V. Modeling the transport of water and ionic tracers in a micrometric clay sample. *Appl. Clay Sci.* **2016**, *123*, 18−28.
(74) Lammers, L. N.; Bourg, I. C.; Okumura, M.; Kolluri, K.; Sposito, G.; Machida, M. Molecular dynamics simulations of cesium adsorption on Illite nanoparticles. *J. Colloid Interface Sci.* **2017**, *490*, 608−620.
(75) Tournassat, C.; Davis, J. A.; Chiaberge, C.; Grangeon, S.; Bourg, I. C. Modeling the acid−base properties of montmorillonite edge surfaces. *Environ. Sci. Technol.* **2016**, *50*, 13436−13445.
(76) Kwon, K. D.; Newton, A. G. Structure and stability of pyrophyllite edge surfaces: Effect of temperature and water chemical potential. *Geochim. Cosmochim. Acta* **2016**, *190*, 100−114.
(77) Tazi, S.; Rotenberg, B.; Salanne, M.; Sprik, M.; Sulpizi, M. Absolute acidity of clay edge sites from ab-initio simulations. *Geochim. Cosmochim. Acta* **2012**, *94*, 1−11.
(78) Liu, X.; Cheng, J.; Sprik, M.; Lu, X.; Wang, R. Interfacial structures and acidity of edge surfaces of ferruginous smectites. *Geochim. Cosmochim. Acta* **2015**, *168*, 293−301.
(79) Ho, T. A.; Greathouse, J. A.; Wang, Y.; Criscenti, L. J. Atomistic Structure of Mineral Nano-aggregates from Simulated Compaction and Dewatering. *Sci. Rep.* **2017**, *7*, 15286.
(80) Jiang, X. Z.; Feng, M.; Luo, K. H.; Ventikos, Y. Large-scale molecular dynamics simulation of flow under complex structure of endothelial glycocalyx. *Comput. Fluids* **2018**, *173*, 140−146.
(81) Bocquet, L.; Charlaix, E. Nanofluidics, from bulk to interfaces. *Chem. Soc. Rev.* **2010**, *39*, 1073−1095.
(82) French, R. H.; Parsegian, V. A.; Podgornik, R.; Rajter, R. F.; Jagota, A.; Luo, J.; Asthagiri, D.; Chaudhury, M. K.; Chiang, Y.-m.; Granick, S.; et al. Long range interactions in nanoscale science. *Rev. Mod. Phys.* **2010**, *82*, 1887−1944.
(83) Richards, L. A.; Schäfer, A. I.; Richards, B. S.; Corry, B. The importance of dehydration in determining ion transport in narrow pores. *Small* **2012**, *8*, 1701−1709.
(84) Lee, J. H.; Guggenheim, S. Single crystal X-ray refinement of pyrophyllite-1Tc. *Am. Mineral.* **1981**, *66*, 350−357.
(85) Pauling, L. The principles determining the structure of complex ionic crystals. *J. Am. Chem. Soc.* **1929**, *51*, 1010−1026.
(86) White, G. N.; Zelazny, L. Analysis and Implications of the Edge Structure of Dioctahedral Phyllosilicates. CLAYS CLAY MINER. *Clays Clay Miner.* **1988**, *36*, 141.
(87) Allen, M. P.; Tildesley, D. J. *Computer simulation of liquids*; Oxford University Press, 1991.
(88) Abraham, M. J.; Murtola, T.; Schulz, R.; Páll, S.; Smith, J. C.; Hess, B.; Lindahl, E. GROMACS: High performance molecular simulations through multi-level parallelism from laptops to supercomputers. *SoftwareX* **2015**, *1*, 19−25.
(89) Cygan, R. T.; Liang, J.-J.; Kalinichev, A. G. Molecular models of hydroxide, oxyhydroxide, and clay phases and the development of a general force field. *J. Phys. Chem. B* **2004**, *108*, 1255−1266.
(90) Berendsen, H. J. C.; Grigera, J. R.; Straatsma, T. P. The missing term in effective pair potentials. *J. Phys. Chem.* **1987**, *91*, 6269−6271.
(91) Smith, D. E.; Dang, L. X. Computer simulations of NaCl association in polarizable water. *J. Chem. Phys.* **1994**, *100*, 3757−3766.
(92) Cebula, D. J.; Thomas, R. K.; Middleton, S.; Ottewill, R. H.; White, J. W. Neutron diffraction from clay-water systems. *Clays Clay Miner.* **1979**, *27*, 39−52.
(93) Gelb, L. D.; Gubbins, K. Pore size distributions in porous glasses: a computer simulation study. *Langmuir* **1999**, *15*, 305−308.
(94) Sarkisov, L.; Harrison, A. Computational structure characterisation tools in application to ordered and disordered porous materials. *Mol. Simul.* **2011**, *37*, 1248−1257.
(95) Torquato, S.; Avellaneda, M. Diffusion and reaction in heterogeneous media: Pore size distribution, relaxation times, and mean survival time. *J. Chem. Phys.* **1991**, *95*, 6477−6489.
(96) Sposito, G.; Prost, R. Structure of water adsorbed on smectites. *Chem. Rev.* **1982**, *82*, 553−573.
(97) Daly, K. B.; Benziger, J. B.; Debenedetti, P. G.; Panagiotopoulos, A. Z. Massively parallel chemical potential calculation on graphics processing units. *Comput. Phys. Commun.* **2012**, *183*, 2054−2062.
(98) Sposito, G. Thermodynamics of swelling clay-water systems. *Soil Sci.* **1972**, *114*, 243−249.
(99) Sato, H. Thermodynamic model on swelling of bentonite buffer and backfill materials. *Physics and Chemistry of the Earth, Parts A/B/C* **2008**, *33*, S538−S543.
(100) Overbeek, J. T. G. On the electrostatic interaction in macroionic solutions and suspensions. *J. Chem. Phys.* **1987**, *87*, 4406−4408.
(101) Smalley, M. V. *Clay swelling and colloid stability*; CRC Press, 2006.

https://dx.doi.org/10.1021/acs.jpcc.9b11197
J. Phys. Chem. C 2020, 124, 3702−3714

(102) Frenkel, D.; Smit, B. *Understanding molecular simulation: from algorithms to applications*; Elsevier, 2001; Vol. *1*.
(103) Carrier, B.; Vandamme, M.; Pellenq, R. J.-M.; Bornert, M.; Ferrage, E.; Hubert, F.; Van Damme, H. Effect of water on elastic and creep properties of self-standing clay films. *Langmuir* **2016**, *32*, 1370−1379.
(104) Ho, T. A.; Criscenti, L. J.; Greathouse, J. A. Revealing Transition States during the Hydration of Clay Minerals. *J. Phys. Chem. Lett.* **2019**, *10*, 3704−3709.
(105) Prost, R.; Koutit, T.; Benchara, A.; Huard, E. State and location of water adsorbed on clay minerals: consequences of the hydration and swelling-shrinkage phenomena. *Clays Clay Miner.* **1998**, *46*, 117−131.
(106) Saiyouri, N.; Hicher, P. Y.; Tessier, D. Microstructural approach and transfer water modelling in highly compacted unsaturated swelling clays. *Mech. Cohesive-Frict. Mater.* **2000**, *5*, 41−60.
(107) Ferrage, E.; Lanson, B.; Sakharov, B. A.; Drits, V. A. Investigation of smectite hydration properties by modeling experimental X-ray diffraction patterns: Part I. Montmorillonite hydration properties. *Am. Mineral.* **2005**, *90*, 1358−1374.
(108) Ferrage, E.; Lanson, B.; Michot, L. J.; Robert, J.-L. Hydration properties and interlayer organization of water and ions in synthetic Na-smectite with tetrahedral layer charge. Part 1. Results from X-ray diffraction profile modeling. *J. Phys. Chem. C* **2010**, *114*, 4515−4526.
(109) Lindholm, J.; Boily, J.-F.; Holmboe, M. Deconvolution of Smectite Hydration Isotherms. *ACS Earth and Space Chemistry* **2019**, *3*, 2490.
(110) Sposito, G. *The surface chemistry of natural particles*; Oxford University Press, 2004.
(111) Molera, M.; Eriksen, T.; Jansson, M. Anion diffusion pathways in bentonite clay compacted to different dry densities. *Appl. Clay Sci.* **2003**, *23*, 69−76.
(112) Muurinen, A.; Karnland, O.; Lehikoinen, J. Ion concentration caused by an external solution into the porewater of compacted bentonite. *Physics and Chemistry of the Earth* **2004**, *29*, 119−127.
(113) Muurinen, A.; Karnland, O.; Lehikoinen, J. Effect of homogenization on the microstructure and exclusion of chloride in compacted bentonite. *Physics and Chemistry of the Earth* **2007**, *32*, 485−490.
(114) Van Loon, L. R.; Glaus, M. A.; Muller, W. Anion exclusion effects in compacted bentonites: Towards a better understanding of anion diffusion. *Appl. Geochem.* **2007**, *22*, 2536−2552.
(115) Fu, M.; Zhang, Z.; Low, P. Changes in the properties of a montmorillonite-water system during the adsorption and desorption of water: hysteresis. *Clays Clay Miner.* **1990**, *38*, 485−492.
(116) Keren, R.; Shainberg, I. Water vapor isotherms and heat of immersion of Na- and Camontmorillonite systems. III. Thermodynamics. *Clays Clay Miner.* **1980**, *28*, 204−210.
(117) Zhang, Z. Z.; Low, P. F. Relation between the heat of immersion and the initial water content of Li-, Na-, and K-montmorillonite. *J. Colloid Interface Sci.* **1989**, *133*, 461−472.
(118) Michot, L. J.; Ferrage, E.; Jimenéz-Ruiz, M.; Boehm, M.; Delville, A. Anisotropic features of water and ion dynamics in synthetic Na- and Ca-smectites with tetrahedral layer charge. A combined quasi-elastic neutron-scattering and molecular dynamics simulation study. *J. Phys. Chem. C* **2012**, *116*, 16619−16633.
(119) Marry, V.; Dubois, E.; Malikova, N.; Durand-Vidal, S.; Longeville, S.; Breu, J. Water dynamics in hectorite clays: Influence of temperature studied by coupling neutron spin echo and molecular dynamics. *Environ. Sci. Technol.* **2011**, *45*, 2850−2855.
(120) Liu, J.; Yamada, H.; Kozaki, T.; Sato, S.; Ohashi, H. Effect of silica sand on activation energy for diffusion of sodium ions in montmorillonite and silica sand mixture. *J. Contam. Hydrol.* **2003**, *61*, 85−93.
(121) Kozaki, T.; Sato, Y.; Nakajima, M.; Kato, H.; Sato, S.; Ohashi, H. Effect of particle size on the diffusion behavior of some radionuclides in compacted bentonite. *J. Nucl. Mater.* **1999**, *270*, 265−272.
(122) Bourg, I. C.; Sposito, G.; Bourg, A. C. M. Tracer diffusion in compacted, water-saturated bentonite. *Clays Clay Miner.* **2006**, *54*, 363−376.
(123) Sato, H.; Ashida, T.; Kohara, Y.; Yui, M.; Sasaki, N. Effect of dry density on diffusion of some radionuclides in compacted sodium bentonite. *J. Nucl. Sci. Technol.* **1992**, *29*, 873−882.
(124) Suzuki, S.; Sato, H.; Ishidera, T.; Fujii, N. Study on anisotropy of effective diffusion coefficient and activation energy for deuterated water in compacted sodium bentonite. *J. Contam. Hydrol.* **2004**, *68*, 23−37.
(125) Sato, H.; Suzuki, S. Fundamental study on the effect of an orientation of clay particles on diffusion pathway in compacted bentonite. *Appl. Clay Sci.* **2003**, *23*, 51−60.
(126) Nye, P. H. Diffusion of ions and uncharged solutes in soils and soil clays. *Adv. Agron.* **1980**, *31*, 225−272.
(127) Fricke, H. A mathematical treatment of the electric conductivity and capacity of disperse systems. *Phys. Rev.* **1924**, *24*, 575−587.
(128) Tournassat, C.; Bourg, I. C.; Steefel, C. I.; Bergaya, F. Surface properties of clay minerals. *Dev. Clay Sci.* **2015**, *6*, 5−31.
(129) Lutterotti, L.; Voltolini, M.; Wenk, H.-R.; Bandyopadhyay, K.; Vanorio, T. Texture analysis of a turbostratically disordered Ca-montmorillonite. *Am. Mineral.* **2010**, *95*, 98−103.
(130) Bourg, I. C.; Tournassat, C. *Developments in Clay Science*; Elsevier, 2015; Vol. *6*; pp 189−226.
(131) Tyagi, M.; Gimmi, T.; Churakov, S. V. Multi-scale microstructure generation strategy for up-scaling transport in clays. *Adv. Water Resour.* **2013**, *59*, 181−195.
(132) Gimmi, T.; Churakov, S. V. Water retention and diffusion in unsaturated clays: Connecting atomistic and pore scale simulations. *Appl. Clay Sci.* **2019**, *175*, 169−183.
(133) Gimmi, T.; Kosakowski, G. How mobile are sorbed cations in clays and clay rocks? *Environ. Sci. Technol.* **2011**, *45*, 1443−1449.
(134) van Schaik, J. C.; Kemper, W. D.; Olsen, S. R. Contribution of adsorbed cations to diffusion in clay-water systems. *Soil Science Society of America Proceedings* **1966**, *30*, 17−22.

https://dx.doi.org/10.1021/acs.jpcc.9b11197
J. Phys. Chem. C 2020, 124, 3702−3714